

NOVEL LINEAR TUBULAR BRUSHLESS PERMANENT MAGNET MOTOR

Z.Q. Zhu¹, P.J. Hor¹, D. Howe¹, and J. Rees-Jones²

¹University of Sheffield, UK.

²Unilever Research Port Sunlight Laboratory, UK

INTRODUCTION

There is an increasing requirement for controlled linear motion over short and long strokes, in the factory automation and packaging industries, for example. Linear brushless PM motors could offer significant advantages over conventional actuation technologies, such as motor driven cams and linkages and pneumatic/hydraulic rams - in terms of efficiency, operating bandwidth, speed and thrust control, stroke and positional accuracy, and indeed over other linear motor technologies, such as induction and switched reluctance motors.

A novel form of linear tubular brushless permanent magnet motor has been developed. The paper describes the principle of operation, alternative topologies of the motor, and potential applications; discusses the main design considerations, such as the back-emf waveform and the cogging force; and compares finite element predictions and measurements.

BASIC MOTOR TOPOLOGIES AND COGGING FORCE CALCULATION

The developed tubular brushless permanent magnet motor has a multi-pole permanent magnet stator, which can have either radially magnetised magnets mounted at the surface of a ferromagnetic rod or axially magnetised magnets and ferromagnetic pole-pieces, and an isolated two-phase iron-cored armature, each phase spanning a pole-pitch and carrying a phase winding controlled by an H-bridge converter. The basic motor topologies are illustrated in Fig.1. The motor topology shown in Fig.1a is more appropriate for brushless ac operation, while that shown in Fig.1b is appropriate for brushless dc operation, due to the fact that their back-emf waveforms are essentially sinusoidal and trapezoidal, respectively. Although it is a longitudinal flux motor, its force production has some similarity to transverse flux PM motors, which have been the subject of recent investigations [1][2]. Since it has a tubular topology, the net radial force is negligible, which minimises demands on the bearing system, and there are no end-windings, which is conducive to low copper loss. Due to its high force/volume and force/ampere capabilities, it is particularly suitable for high-force direct-drive applications.

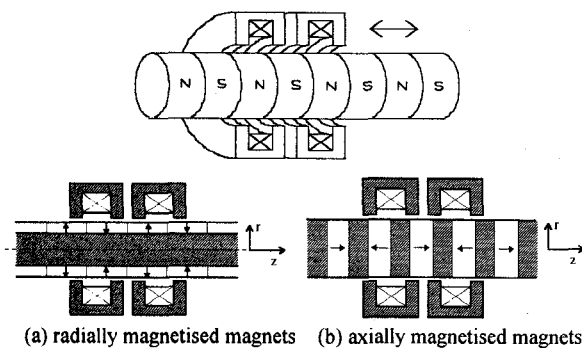


Fig.1 Basic topologies of 2-phase tubular linear brushless permanent magnet motor.

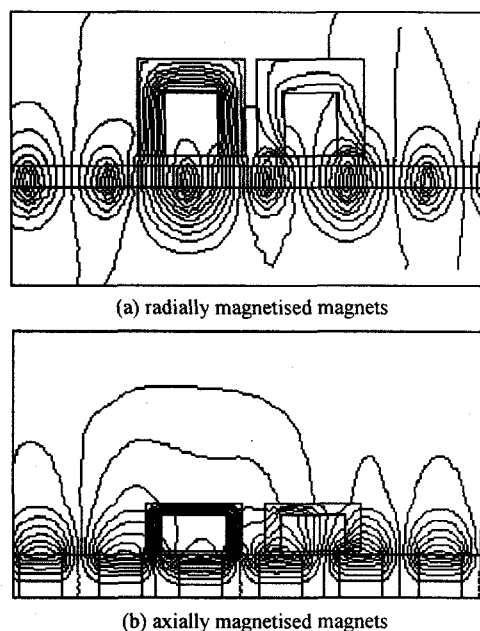


Fig.2 Open-circuit field distributions.

Typical open-circuit field distributions for the basic motor topologies are shown in Fig.2. Since the tooth-pitch of the armature is equal to the pole-pitch, both the tooth ripple and end-components of cogging force have identical wavelengths, viz. one pole-pitch. Thus, if the mutual magnetic coupling between the two phases is neglected, the resultant cogging force can be cancelled completely if the cogging force waveform associated with one phase is designed to be symmetrical about its peak, since the two cogging force waveforms are in

antiphase. It will be evident that two phases (rather than any other phase number) are necessary in order to achieve this electromagnetic balance between phases. However, as will be shown later, due to mutual magnetic coupling, design optimisation is necessary in order to minimise the resultant cogging force.

Although the cogging force can be determined solely from finite element analysis, it is not appropriate for determining the resultant cogging force waveform or the motor dimensions so as to minimise cogging, since it is relatively time consuming. Instead, a finite element/analytical based technique is employed.

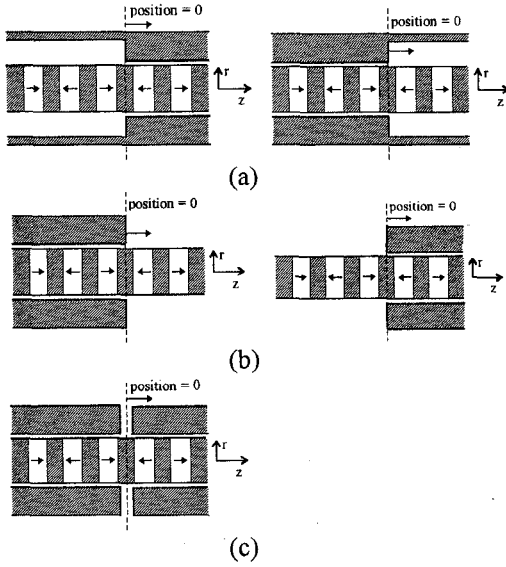


Fig.3 Basic structures for cogging force synthesis.

Since the tooth pitch is equal to one pole-pitch, the technique assumes that the cogging force component which is associated with a single edge of a stator tooth is independent of the force components which are associated with all the other edges. The resultant cogging force can then be synthesised from the force components associated with the basic structures shown in Fig.3, each of which can be pre-calculated, by finite element analysis. Calculated waveforms for Prototype Motor 1 are shown in Fig.4, the leading design parameters being given in the Appendix. Clearly, due to symmetry, $F_1(-z)$ is a mirror image of $F_1(z)$, and similarly for F_2 .

The resultant cogging force is then synthesised analytically from the calculated cogging force components, by utilising symmetry and introducing appropriate phase shifts. For example, for a single-phase stator core,

$$F_c = F_1(z) - F_2(-(z+l_t)) + F_2(z+l_t+l_s) - F_1(-(z+2l_t+l_s)) \quad (1)$$

where $\tau = l_t + l_s$ is the pole-pitch, and l_t and l_s are the tooth width and slot width, respectively.

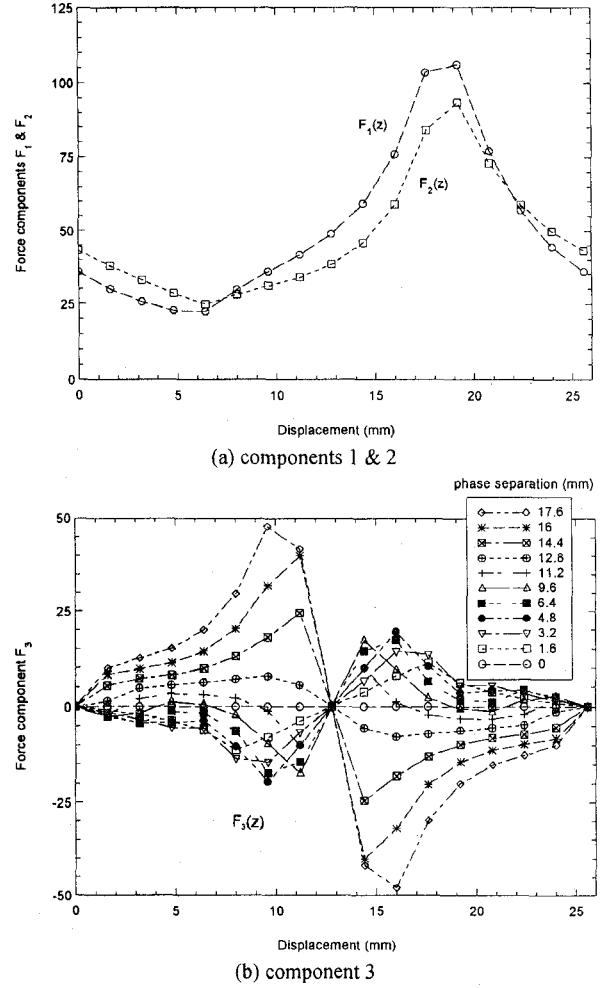


Fig.4. Finite element calculated force waveforms for the three basic structures shown in Fig.3.

The above synthesis process is demonstrated in Fig.5 for a single-phase core. The resultant cogging force for two phases can be synthesised in a similar way.

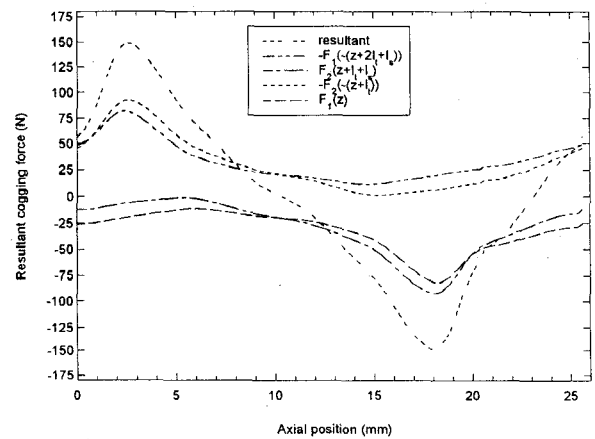


Fig.5. Synthesis of cogging force from force components for a single phase core of Motor 1.

Fig.6 compares measured, finite element predicted and analytically synthesised cogging force waveforms for both a single phase and for two phases. As will be seen,

good agreement is achieved. However, it was found [3] that when the tooth width is made narrower the higher saturation causes the peak of the analytically synthesised cogging force waveform to be slightly displaced relative to the finite element and measured waveforms. However, the accuracy of both the waveform and amplitude of the cogging force is still relatively good, for both a single phase and two phases.

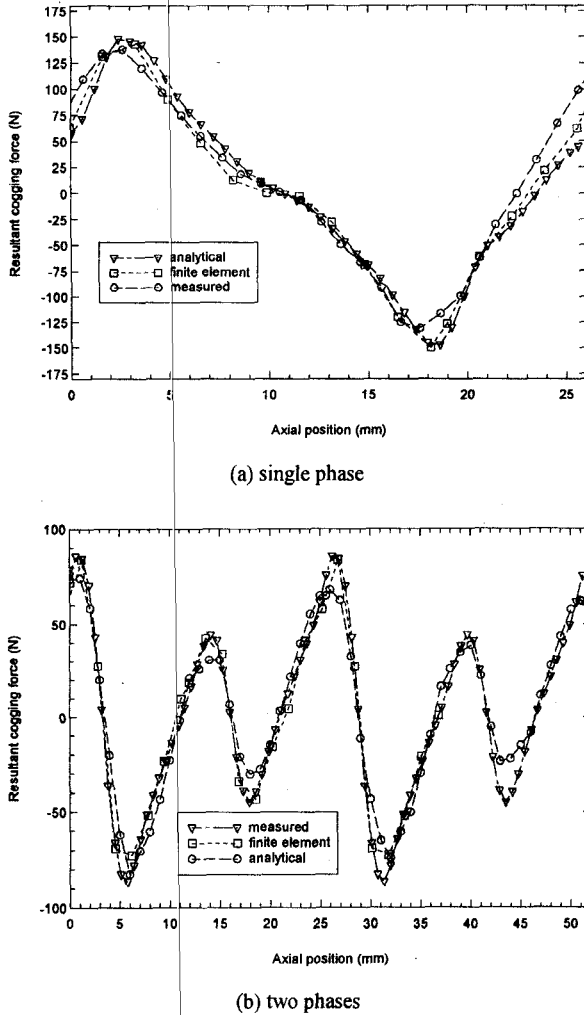


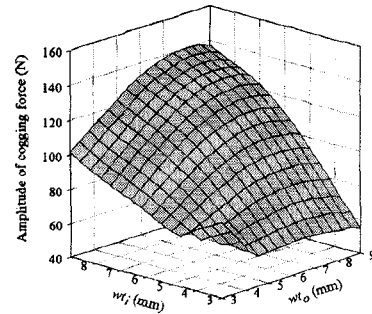
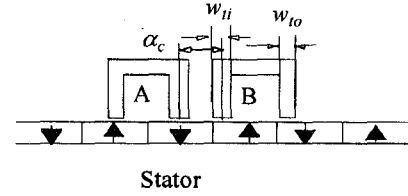
Fig.6 Comparison of measured, finite element predicted, and analytically synthesised cogging force waveforms for Motor 1.

Since the basic magnetic structures are simple and applicable irrespective of the dimensions and configuration of the armature, the developed technique can be used to assess the relative merits of alternative motor designs and topologies, and thereby to aid the minimisation of the resultant cogging force, as will be described in the next section.

ALTERNATIVE MOTOR STRUCTURES AND COGGING FORCE MINIMISATION

In order to illustrate the application of the developed method of cogging force calculation, Fig.7 shows the variation of resultant cogging force with the inner and

outer tooth widths of the basic motor topology. It will be seen that the resultant cogging force is large, even when the cogging force is minimised. However, there are a number of possible variants to the basic motor topology, which can exhibit a lower cogging force, as will be shown later. For example, each phase set in Fig.8a comprises a number of series-connected coils in order to increase the resultant thrust force, whilst each phase set in Fig.8b has a multi-slotted iron core. However, the slot pitch is still one pole-pitch, and the developed finite element/analytical method for predicting the cogging force can still be used to aid their design optimisation for minimum cogging force.



$$\alpha_c = \frac{1}{2} \tau_c$$

Fig.7 Variation of cogging force with inner and outer tooth widths.

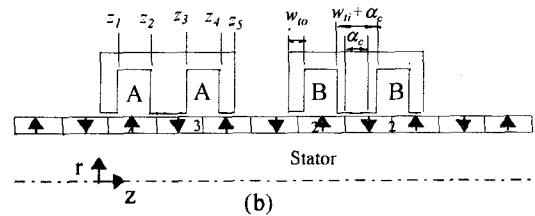
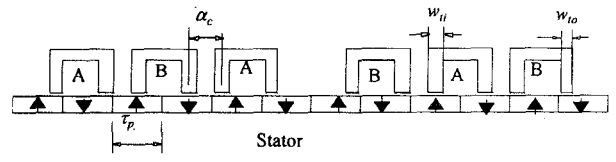


Fig.8 Alternative motor structures for optimisation.

For example, the cogging force waveform due to phase set A of the motor shown in Fig.8b is given by:

$$F_{cA} = F_1(z) - F_2(-z + z_1) + F_2(z - z_2) - F_2(-z + z_3) + F_2(z - z_4) - F_1(-z + z_5) \quad (2)$$

where F_1 , F_2 are pre-calculated cogging force components associated with the inner and outer edges of

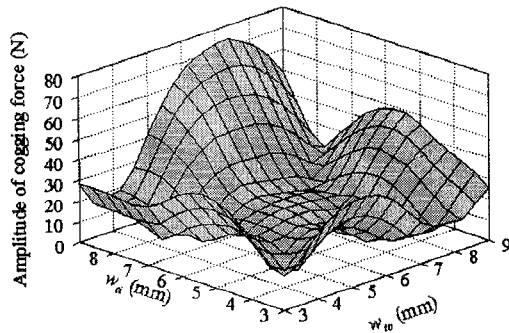
the iron teeth, and z_1, z_2, z_3, z_4 and z_5 are their relative axial locations. The cogging force associated with phase set B is related to that of phase set A by:

$$F_{cB}(z) = F_{cA}(z - 7/2\tau_p) \quad (3)$$

Hence, the resultant cogging force is obtained from:

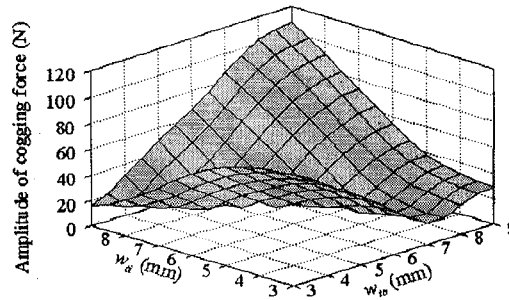
$$F_c = F_{cA} + F_{cB} \quad (4)$$

The objective is to make the F_{cA} and F_{cB} cogging force waveforms have, as close as possible, quarter symmetry so that equation (4) yields minimum cogging force. For both motors, the parameters α_c , w_{to} and w_{ti} are scanned, and for each combination the maximum cogging force is calculated. The optimum value of α_c is found to be $1/3$ pole-pitch. In contrast, the optimum value of α_c for the motor topology shown in Fig.8a is $2/3$ pole-pitch. The variation of the cogging force amplitudes is shown in Figs.9 and 10.



$$\alpha_c = 2/3 \tau_c$$

Fig.9 Variation of cogging force with leading design parameters for motor topology shown in Fig.8a.



$$\alpha_c = 2/3 \tau_c$$

Fig.10 Variation of cogging force with leading design parameters for motor topology shown in Fig.8b.

Based on the above results, a prototype Motor 2, whose leading design parameters are given in the Appendix, was built. Fig.11 shows the corresponding measured cogging force waveform. As can be seen, the amplitude of the cogging force is small, $< 5\%$ of the rated force. Other performance parameters are given in the next section.

ELECTROMAGNETIC PERFORMANCE

Prototype Motor 2 was operated from a DC link voltage of 160V, and produced rated force of 175N at a rated phase current of 5A. It has an emf constant of 24 V/ms^{-1} . Fig.12 shows an open-circuit field distribution, while Figs.13 and 14 show predicted and measured flux-linkage and emf waveforms, respectively. Both are essentially sinusoidal, the emf having less than 2 percent harmonic content. The measured flux-linkage waveform is slightly lower than the predicted value, primarily due to the form of construction of the slotted armature, which is laminated and circumferentially consists of four sections similar to that described in [4].

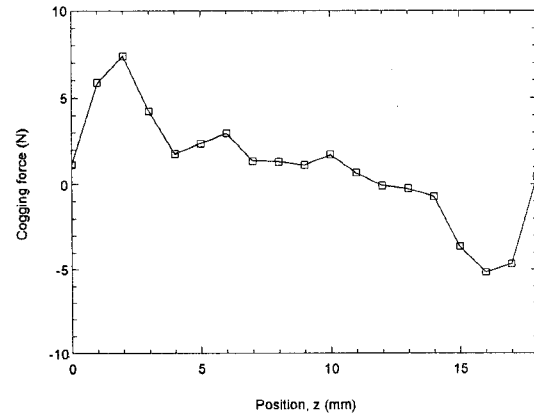


Fig.11 Measured cogging force waveform of Motor 2.

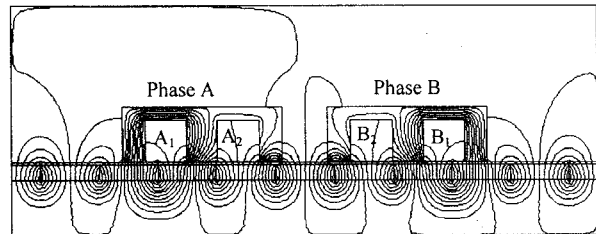


Fig.12 Open-circuit field distribution of Motor 2.

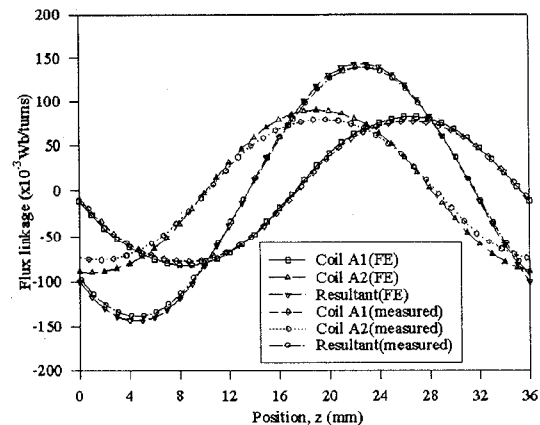


Fig.13 Measured and predicted phase flux-linkage waveforms of Motor 2.

The force/volume, force/active mass, airgap shear stress and force constant are 244kN/m^3 , 121N/kg , 11.0kN/m^2 and 24N/A , respectively. Its dynamic performance has been simulated using Matlab/Simulink, with the zero d-axis current control. The results [5] show that the motor is capable of an acceleration of $4g$ when carrying a 2 kg payload.

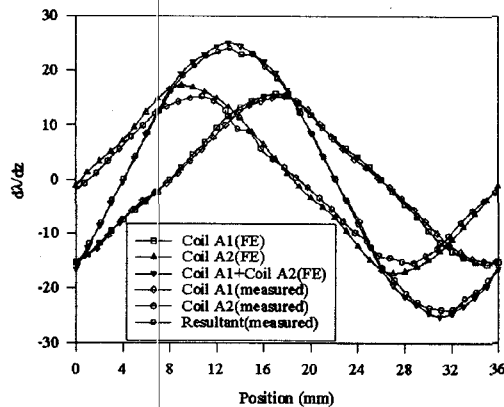


Fig.14 Back-emf waveforms of Motor 2.

CONCLUSIONS

A novel long-stroke linear tubular slotted brushless permanent magnet motor has been developed. It is a longitudinal flux motor with a slot-pitch approximately equal to one pole-pitch, and a similar force production capability as a transverse flux PM motor. A combined finite element/analytical technique has been developed to aid the minimisation of the cogging force to $< 5\%$ of rated force. The force/volume, force/active mass, airgap shear stress and force constant are 244kN/m^3 , 121N/kg , 11.0kN/m^2 and 24N/A , respectively. Due to its high force/volume and force/ampere capabilities, it has potential for high-force direct-drive applications.

ACKNOWLEDGEMENTS

The authors acknowledge the supports of Unilever Research Port Sunlight Laboratory, UK, R & D Laboratory, Daido Steel Co. Ltd., Japan, and University of Science, Malaysia.

APPENDIX - LEADING PARAMETERS OF PROTOTYPE MOTORS

Prototype Motor 1 is based on the motor topology shown in Fig.1b. It has axially magnetised, sintered NdFeB magnets, whose remanence and relative recoil permeability are 1.03T and 1.05 , respectively. The major dimensions are: pole-pitch = 25.6mm , axial magnet thickness = 14mm , axial length of pole-pieces = 11.6mm , outside diameter of thrust rod = 23.4mm , outside diameter of C-core back iron = 50mm , C-core pitch = one pole-pitch, and core tooth widths = 5mm .

Prototype Motor 2 is the optimised design of the motor topology shown in Fig.8b. It has surface-mounted radially magnetised extruded NdFeB magnets, whose remanence and relative recoil permeability are 1.17T and 1.05 , respectively. The pole-pitch = 18mm and the airgap = 1mm , while the outside and inside diameters of the magnet are 42.8mm and 32.8mm respectively. Other optimal dimensions are $w_g=3.6\text{mm}$, $w_{to}=7\text{mm}$, and $\alpha_c=6\text{mm}$.

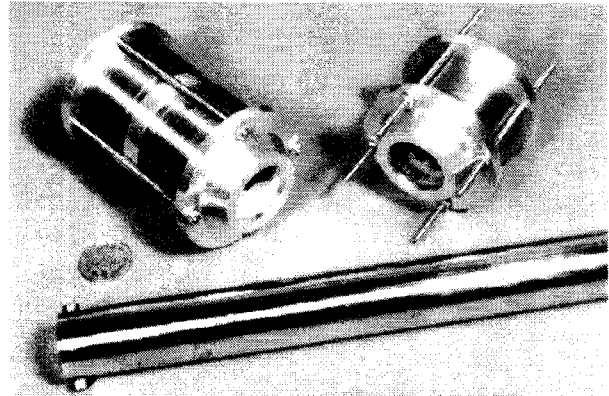


Fig.15 Prototype Motor 1.

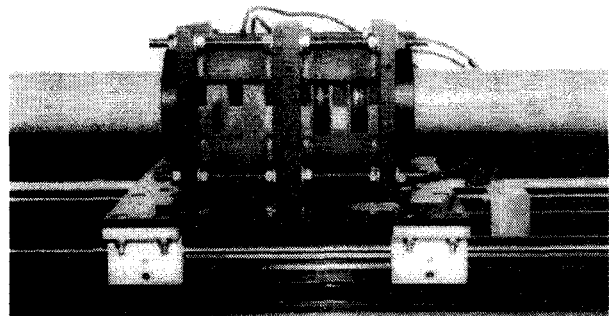


Fig.16 Prototype Motor 2.

REFERENCES

1. Weh H., 1995, "Transverse flux machines in drive and generator application", *Proc. IEEE Power Tech'95 Conference, Sweden*, 75-80.
2. Harris M.R., Pajooman G.H., Sharkh S.M., 1996, "Performance and design optimisation of electric motors with heteropolar surface magnets and homopolar windings", *Proc. IEEE-B*, 143, 429-436.
3. Zhu Z.Q., Hor P.J., Howe D., Rees-Jones J., 1997, "Calculation of Cogging Force in a Novel Slotted Linear Tubular Brushless Permanent Magnet Motor", *Proc. Intermag97, New Orleans, USA*, Paper No. BC-07.
4. Eastham J.F., Akmese R., Lai H.C., 1990, "Optimum design of brushless tubular linear machines", *IEEE Trans. Magnetics*, 26, 2547-2549.
5. Hor P.J., Churn, P., Zhu Z.Q., Howe D., Rees-Jones J., 1997, "Dynamic simulation of novel two-phase permanent magnet linear motor", to be presented at *2nd Int. Conf. Power Electronics and Motion Control*, Hangzhou, China.